



**HAL**  
open science

# Anion Exchange Membranes with High Power Density and Energy Efficiency for Aqueous Organic Redox Flow Batteries

Misgina Tilahun Tsehaye, Xian Yang, Tobias Janoschka, Martin Hager, Ulrich Schubert, Emilie Planes, Fannie Alloin, Cristina Iojoiu

► **To cite this version:**

Misgina Tilahun Tsehaye, Xian Yang, Tobias Janoschka, Martin Hager, Ulrich Schubert, et al.. Anion Exchange Membranes with High Power Density and Energy Efficiency for Aqueous Organic Redox Flow Batteries. *Electrochimica Acta*, 2023, 438, pp.141565. 10.1016/j.electacta.2022.141565 . hal-03656369v2

**HAL Id: hal-03656369**

**<https://hal.science/hal-03656369v2>**

Submitted on 26 Nov 2022

**HAL** is a multi-disciplinary open access archive for the deposit and dissemination of scientific research documents, whether they are published or not. The documents may come from teaching and research institutions in France or abroad, or from public or private research centers.

L'archive ouverte pluridisciplinaire **HAL**, est destinée au dépôt et à la diffusion de documents scientifiques de niveau recherche, publiés ou non, émanant des établissements d'enseignement et de recherche français ou étrangers, des laboratoires publics ou privés.

# Anion exchange membranes with high power density and energy efficiency for aqueous organic redox flow batteries

Misgina Tilahun Tsehay<sup>a,#</sup>, Xian Yang<sup>b,c,d, #</sup>, Tobias Janoschka<sup>d</sup>, Martin D. Hager<sup>b,c</sup>, Ulrich S. Schubert<sup>b,c</sup>, Emilie Planes<sup>a</sup>, Fannie Alloin<sup>a</sup>, Cristina Iojoiu<sup>a,\*</sup>

<sup>a</sup> Univ. Grenoble Alpes, Univ. Savoie Mont Blanc, CNRS, Grenoble INP, LEPMI, 38 000 Grenoble, France

<sup>b</sup> Laboratory of Organic and Macromolecular Chemistry (IOMC), Friedrich Schiller University Jena, Humboldtstrasse 10, 07743 Jena, Germany

<sup>c</sup> Center for Energy and Environmental Chemistry Jena (CEEC Jena), Friedrich Schiller University Jena, Philosophenweg 7a, 07743 Jena, Germany

<sup>d</sup> JenaBatteries GmbH, Otto-Schott-Strasse 15, 07745 Jena, Germany

Corresponding authors:

[Cristina.iojoiu@lepmi.grenoble-inp.fr](mailto:Cristina.iojoiu@lepmi.grenoble-inp.fr)

[Fannie.Alloin@lepmi.grenoble-inp.fr](mailto:Fannie.Alloin@lepmi.grenoble-inp.fr)

[Tobias.janoschka@jenabatteries.de](mailto:Tobias.janoschka@jenabatteries.de)

<sup>#</sup>: Authors contributed equally.

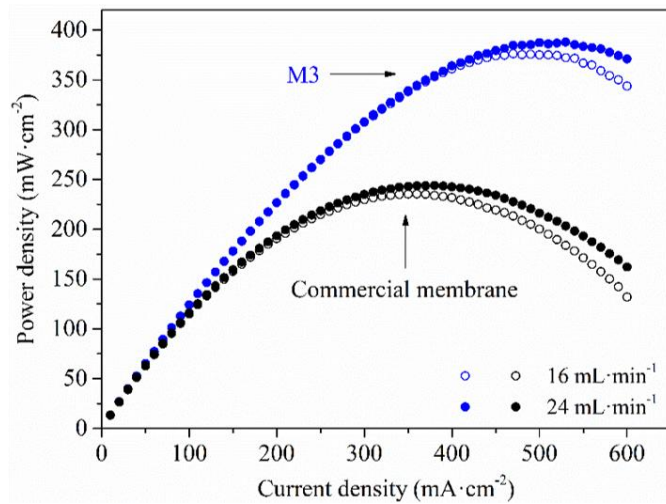
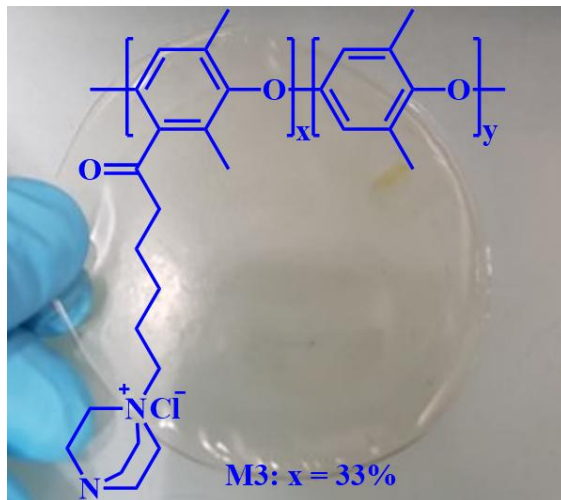
## Abstract

Membrane development in organic redox flow batteries (ORFBs) is of significant importance. Herein, we designed a series of anion exchange membranes made from poly(*p*-phenylene oxide) (PPO) with different degrees of functionalization, cationic moieties and crosslinking degrees. We tested them in a *N,N,N*-2,2,6,6-heptamethylpiperidinyloxy-4-ammonium chloride/1,1'-dimethyl-4,4'-bipyridinium dichloride (TMA-TEMPO/MV) based ORFB single cell to investigate the structure-property-performance relationship. The common problem of active species crossover is solved by controlling the membrane water uptake below 70 wt.%, resulting in stable systems with coulombic efficiency of over 99.3%. The cell employing a membrane prepared from PPO and trimethylamine moiety attached via a C6-spacer achieved the best overall cell performance. It delivered high capacity retention (94% after over 100 consecutive cycles) and higher peak power density (293 mW·cm<sup>-2</sup> at 16 mL·min<sup>-1</sup>) and energy efficiency (80%) than the commercial reference membrane FAA-3-50.

**Keyword:** Anion exchange membranes, aqueous organic redox flow battery, TMA-TEMPO, methyl viologen, power density, energy efficiency

## Graphical abstract

By controlling the water uptake below 70 wt.% and involving a C6 spacer, the obtained membranes maintain excellent ion selectivity and conductivity, resulting in enhanced battery performance that breaks through the commercial membrane.



# 1. Introduction

Redox flow batteries (RFBs) are rechargeable batteries with decoupling of energy and power, where redox-active materials are dissolved in suitable solvents and pumped through the electrodes. RFBs represent one of the most promising technologies for stationary energy storage [1–4]. They are expected to be in high demand as international climate initiatives, such as the European Green Deal, aiming to make our society climate neutral by using intermittent energy sources [5]. To date, a large array of different flow battery systems has been reported, among which the vanadium redox flow battery (VRFB) was industrialized at first and remained leading the flow battery market [6,7]. Nowadays, organic redox flow battery (ORFB) systems have drawn extensive attention because of the ever-growing need for sustainable development. In particular, water-based aqueous organic redox flow batteries (AORFBs) represent promising candidates as they omit critical metals [8,9]. Limited by the electrochemical stability window of water ( $\sim 1.23$  V), most efforts on AORFB development have been focused on creating redox-active species with high solubility and stability aiming for enhanced energy density [8,10].

As another key component, membrane development is of equal importance. However, it requires differentiated emphases with respect to a particular electrochemical system. For instance, researchers have attempted to reduce the cost of VRFB systems by finding cheaper alternatives to replace Nafion<sup>®</sup> [11–13]. For hybrid RFBs involving hazardous or corrosive materials like bromine, high membrane chemical stability is required to withstand the harsh condition [14]. In organic systems, however, membrane development has usually been overlooked as in most cases commercial membranes are used to gain a first insight into the properties of newly developed redox-active materials [15–17]. Recently, a number of systematic studies on the properties of commercial membranes, aiming to boost the cell performance in ORFB systems were published [18,19]. Nevertheless, the exact chemical structures of commercially available membranes are usually not publicly disclosed, making it increasingly difficult to further enhance the performance of a battery system from the perspective of membranes. Overall, the synthesis of an appropriate membrane at a low-cost combining high ionic conductivity and selectivity is of utmost importance for widespread adoption and commercialization of high-performance, efficient and stable AORFBs [8].

As a consequence, in a previous work, we studied the interrelation between the properties of poly(*p*-phenylene oxide) (PPO) based anion exchange membranes (AEMs) and corresponding cell performance in an ORFB single cell using *N,N,N*-2,2,6,6-heptamethylpiperidinyloxy-4-ammonium chloride and 1,1'-dimethyl-4,4'-bipyridinium dichloride as active species (TMA-TEMPO/MV) [20], see the half-cell reactions in Figure S1. Detailed information on the solubility behavior of TMA-TEMPO and MV is

discussed in elsewhere [15]. A high ion exchange capacity (IEC), low water uptake and high chloride ion conductivity were identified as key parameters for preparing AEM with a good battery efficiency and performance. However, in the study, only the impact of IECs on the overall cell performance was investigated, thus the impact of other key parameters, such as crosslinking vs linear nature, use of spacer between polymer backbone and ionic function and type of cation require further investigation.

Inspired by our recent findings, we here envisioned a TMA-TEMPO/MV based AORFB featuring a pH-neutral electrolyte with high energy efficiency, peak power density and excellent coulombic efficiency by preparing and employing AEM with optimized water uptake and high chloride conductivity. In this work, we further investigate how the choice of the cationic moiety, the presence of a spacer, IEC value and the polymer crosslinking degree will reflect upon the final cell performance. A series of flexible AEMs composed of PPO functionalized either with 1,4-diazabicyclo-[2.2.2]-octane (DABCO) or trimethylamine (TMA) were fabricated. DABCO and TMA were chosen because of their commercial availability, straightforward functionalization protocols and chemical stabilities in neutral pH systems. In addition, DABCO has the possibility of preparing cross-linked architectures due to its two reactive sites. Most of the prepared membranes employ a spacer between the polymer backbone and cation moiety in order to provide a nanophase separated morphology with well-defined ionic channels [21] and in order to tune the hydrophobicity of the membranes. For the purpose of comparison, the well-performing commercial FAA-3-50 membrane was used as a reference.

## 2. Experimental

### 2.1. Materials

Poly(2,6-dimethyl-1,4-phenyleneoxide) (PPO) ( $M_n = 20,000$ ,  $D = 2.5$ ) was purchased from Polysciences Inc. Methanol (99.9%) was purchased from Fisher Scientific. *N*-Bromosuccinimide (NBS) (99%), 2,2'-azobis(2-methylpropionitrile) (AIBN) (98%), tetrahydrofuran (THF, ACS, >99%), 6-bromohexanoyl chloride (97%), diethyl ether (99+%), chloroform-d ( $CDCl_3$ -d, 99.9% D) and 1,4-diazabicyclo[2.2.2]octane (98%, DABCO) were purchased from Sigma-Aldrich. Dimethyl sulfoxide- $d_6$  (DMSO- $d_6$ , 99.9%),  $AlCl_3$  (98.5%, anhydrous), *N,N*-dimethylacetamide (DMAc, 99.0%) and *N*-methyl-2-pyrrolidone (NMP, reagent grade) were supplied from Acros Organics. Chlorobenzene (ACS reagent,  $\geq 99.5\%$ ) and trimethylamine (TMA, 1 M soln. in THF) was bought from Alfa Aesar. MV and TMA-TEMPO were provided by JenaBatteries GmbH. All chemicals were used as received. The FAA-3-50 AEM was purchased from Fumatech GmbH.

## 2.2. Polymer synthesis

In order to introduce the cation, commercial PPO ( $M_n = 20,000 \text{ g}\cdot\text{mol}^{-1}$ ,  $D = 2.5$ ) was first brominated either by the bromination of benzylic methyl resulting in bromomethylated PPO (PPO-Br) or by acylation resulting in bromohexanone PPO with a six-carbon pendant chain spacer (PPO-6CO-Br).

PPO-6CO-Br: The synthesis was carried out based on a slight modification of the method described by Hibbs [22] and Parrondo *et al.* [23]. PPO-6CO-Br polymers with 57, 33 and 15% degree of bromination were prepared. In a representative example for PPO-6CO-Br with 33% degree of bromination, 5 g PPO (41.67 mmol polymer repetitive units) was dissolved in 200 mL of chlorobenzene in a round bottom flask and flushed with argon. The reaction flask was chilled in an ice bath for about 30 min. Subsequently, 9.6 mL of 6-bromohexanoyl chloride (62.7 mmol) and 2.5 g of  $\text{AlCl}_3$  (Lewis acid catalyst, 18.75 mmol) were added. Finally, the ice bath was removed, and the stirred reaction mixture was allowed to react at room temperature for 24 h followed by precipitation in methanol (1 L) to obtain the PPO-6CO-Br polymer. It was then dried under vacuum at 60 °C for 24 h. A white solid product was obtained (7.2 g, 97.3% yield). The polymer showed approximately 0.33 mol of bromomethyl groups per polymer repeats unit. The protocol is summarized in Scheme 1. A similar protocol was followed to prepare the PPO-6CO-Br polymer with 57% and 15% degree of functionalization. To obtain the PPO-6CO-Br with 57% degree of bromination, the same amounts of 6-bromohexanoyl chloride and  $\text{AlCl}_3$  were used to brominate 2.5 g of PPO. Whereas, for the bromination of PPO-6CO-Br with 15% degree, 4.8 mL 6-bromohexanoyl chloride and 1.25 g  $\text{AlCl}_3$  were used for 5 g PPO. The degree of bromination/functionalization was determined by  $^1\text{H}$  NMR spectroscopy.

PPO-Br: PPO was brominated using NBS as brominating agent and AIBN as initiator in a free-radical bromination [24]. First, 3 g of PPO (25 mmol repeat units) was dissolved in 30 mL chlorobenzene. 1.79 g of NBS (11.05 mmol) and 0.099 g of AIBN (0.6 mmol) were added. After 3 h of reaction under reflux, the reaction mixture was precipitated in an excess of methanol (300 mL) and formed a light-brown precipitate of PPO-Br. The PPO-Br polymer was filtered and dried in a vacuum oven at 60 °C for 24 h before use. The degree of bromination (26.5%) was calculated from the  $^1\text{H}$  NMR spectrum.

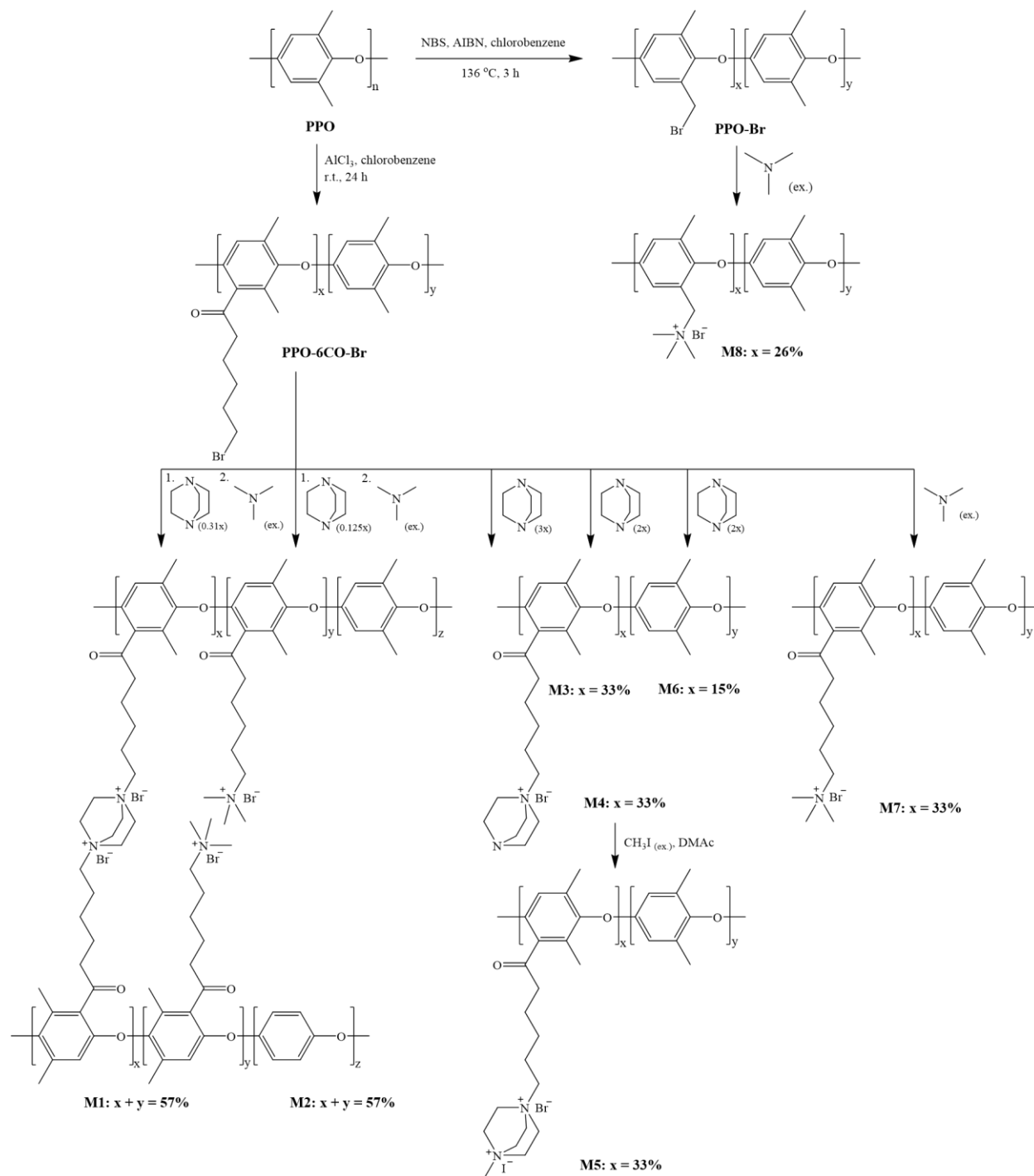
## 2.3. Fabrication of membranes

In total, eight membranes were prepared and named from M1 to M8. Table 1 summarizes the composition and nomenclature of the membranes. For the cross-linked membranes M1 and M2, simultaneous quaternization and membrane preparation procedure were followed. The ratio between the quantity of bromomethyl groups in the PPO-6CO-Br polymer and DABCO was varied to yield membranes with different degrees of crosslinking. In a representative example to prepare M1 using PPO-6CO-Br polymer

with degree of functionalization of 57%, 0.15 g of PPO-6CO-Br (0.387 mmol Br units) was dissolved in DMAc (2 mL). Subsequently, 13.5 mg DABCO (0.12 mmol, in solution of 1 mL DMAc) was added dropwise under stirring for 40 min at 80 °C to initiate the quaternization reaction. In the next step, the prepared solution mixture was degassed under reduced pressure, poured onto a 5 cm diameter petri dish and kept at 60 °C in an oven for 24 h to ensure the simultaneous quaternization reaction and cross-linking. In order to transform the remaining Br units to ammonium, the dry membrane was immersed in deionized water containing 3 equivalents of TMA/Br units in PPO-6CO-Br for 24 h. A similar procedure was followed for the synthesis of M2 membrane: 0.125 mmol of DABCO for 1 mmol Br units in the polymer was used. As shown in Scheme 1, a typical structure is where both DABCO amines are reacted with two CH<sub>2</sub>Br units on two different polymer chains. However, it must be noted that there might be a case where DABCO is reacted only on one site and/or reacted with two CH<sub>2</sub>Br units on the same polymer chains.

For the linear polymers DABCO-based membranes M3 to M6, a different procedure was followed. The PPO-6CO-Br polymer with 33%-degree of bromination were dissolved in DMAc (7wt./v%). DABCO was added in excess (see Table 1) under high stirring to avoid crosslinking. The solution containing the polymer and DABCO was stirred for 24 h and then poured directly onto a petri dish to cast the membrane. The petri dish was kept in an oven at 60 °C for 24 h to evaporate the solvent and form a solid film. To remove the excess amines and remaining solvents, the dried membranes were soaked in deionized water for 24 h. To prepare M5, dry M4 was re-dissolved in DMAc and an excess iodomethane was added to quaternize the free tertiary amine. For M6, PPO-6CO-Br polymer with lower degree of bromination (15%) was used.

For the TMA-based membranes M7 and M8, the brominated polymers were first dissolved in the respective solvents (7 wt./v%); PPO-6CO-Br in DMAc and PPO-Br in NMP (as the polymer was not completely soluble in DMAc). For example, to prepare M7, 0.15 g of PPO-6CO-Br was dissolved in DMAc (7 wt./v %), and TMA (3% molar excess with respect to the Br units in the polymer) was added. The procedures followed to prepare the membranes are schematically represented in Scheme 1.



Scheme 1: Schematic representation of the syntheses of AEMs based on PPO-Br and PPO-6CO-Br polymer backbones. Bromide and iodine ions in the final membranes were replaced by chloride ions for further characterizations and cell tests.



Table 1: Composition and nomenclature of the AEM prepared.

Membrane	Polymer (degree of bromination)	Cation	Reaction ratio: (mol amine)/(mol Br units in the polymer)
M1	PPO-6CO-Br (57%)	DABCO + TMA	0.31 + (3)*
M2	PPO-6CO-Br (57%)	DABCO + TMA	0.125 + (3)*
M3	PPO-6CO-Br (33%)	DABCO	3
M4	PPO-6CO-Br (33%)	DABCO	2
M5	PPO-6CO-Br (33%)	DABCO	2 + **
M6	PPO-6CO-Br (15%)	DABCO	2
M7	PPO-6CO-Br (33%)	TMA	3
M8	PPO-Br (26%)	TMA	3

\* Values in brackets are amount of TMA used with respect to the Br units in the polymer

\*\* Methylated with excess iodomethane

## 2.4. Characterizations

### 2.4.1. Structural characterization

<sup>1</sup>H NMR spectroscopy was used to determine the membrane's polymer structures. A Bruker AV 400 NMR spectrometer was used to record the <sup>1</sup>H NMR spectra. DMSO-d<sub>6</sub> ( $\delta = 2.50$  ppm) or CDCl<sub>3</sub> ( $\delta = 7.26$  ppm) were used as solvents.

### 2.4.2. Chloride ion conductivity

The prepared membranes were converted to Cl<sup>-</sup> form by exchanging the original Br<sup>-</sup> form of resulting membranes in a saturated NaCl (1 M) aqueous solution at room temperature for 48 h, followed by immersion in deionized water overnight to remove the excess of salt. The conductivity of the membranes was measured via the through-plane impedance technique using a homemade measuring cell and a HP response analyzer by two-point probe impedance method in the AC frequency ranging from 13 MHz to 5 Hz.

The conductivity was calculated accordingly to equation (1):

$$\sigma = \frac{L}{R \times A} \quad (1)$$

Where  $\sigma$  is the ionic conductivity (S·cm<sup>-1</sup>), L (cm) is the distance between the electrodes (wet membrane thickness), R ( $\Omega$ ) is the resistance of the membrane obtained at high frequency and A (cm<sup>2</sup>) is the membrane active area (0.0314 cm<sup>2</sup>). To obtain membrane resistance, cell resistance is first measured

without membrane and then subtracted from the cell resistance with membrane. The average of at least three measurements was used to calculate the ionic conductivity.

### 2.4.3. Ionic exchange capacity and water uptake

The IEC ( $\text{mmol}\cdot\text{g}^{-1}$ ), *i.e.*, the number of charged functional groups per gram of polymer, was measured by Mohr titration method [25]. Therefore, the membranes were converted to  $\text{Cl}^-$  form as discussed above. Membrane samples ( $\sim 0.05$  g) were dried in a vacuum oven at  $50^\circ\text{C}$  for 24 h. The dry weight of the membranes was recorded before immersion in 0.5 M aq.  $\text{Na}_2\text{SO}_4$  (25.00 mL), followed by replacing the  $\text{Cl}^-$  anions contained in the membranes with  $\text{SO}_4^{2-}$ , for at least 48 h under stirring. Three samples of the resulting solution (containing released  $\text{Cl}^-$  ions) were titrated with 0.01 M aq.  $\text{AgNO}_3$ .  $\text{K}_2\text{CrO}_4$  was used as an indicator. The IEC of the membranes is calculated using the following equation (2):

$$IEC = \frac{\text{Volume of AgNO}_3 \text{ (mL)} \times \text{Concentration of AgNO}_3 \text{ (mmol/mL)}}{\text{g (weight of dry membrane)}} \quad (2)$$

Water uptake (WU) of the membrane after immersion in water at room temperature for 24 h is calculated using the weight of the dry and wet membrane samples. The WU of the membrane is calculated using equation (3):

$$WU(\%) = \frac{W_{wet} - W_{dry}}{W_{dry}} \times 100 \quad (3)$$

The hydration number (or membrane water concentration) ( $\lambda$ ), defined as the number of water molecules per ionic group, is calculated from equation (4):

$$\lambda = \left( \frac{W_{wet} - W_{dry}}{18.01} \right) \left( \frac{1000}{IEC \times W_{dry}} \right) = \frac{WU(\%) \times 10}{IEC \times 18.01} \quad (4)$$

### 2.4.4. Degree of crosslinking

The degree of crosslinking of M1 and M2 membranes was calculated from the feed ratio of DABCO (crosslinker) and brominated polymer using the following equation (5) [26]:

$$\text{Degree of crosslinking}(\%) = \frac{n_{DABCO}}{n_{Br}/2} \times 100 \quad (5)$$

Where  $n_{DABCO}$  and  $n_{Br}$  are the amounts of DABCO (mol) added and bromine groups (mol) in the polymer, respectively.

### 2.4.5. Atomic force microscopy (AFM)

After being soaked with a drop of water, the membrane sample surfaces were immediately imaged at room temperature and 40 to 60% relative humidity using a Nanowizard (JPK) of CIME Nanotech platform (Grenoble, France). Experiments were performed in the tapping mode using Si probes with 5

$\text{N}\cdot\text{m}^{-1}$  spring constant and resonance frequencies in the range 60 to 80 kHz. Phase and height images were recorded simultaneously. The images were acquired in hard tapping conditions: the interaction of the tip with the specimen was adjusted by the ratio of the set point ( $A_{sp}$ ) to the free oscillation amplitude ( $A_0$ ), to obtain a ratio  $A_{sp}/A_0$  equal to 0.7 to 0.8. Under these operating conditions, the morphology of the samples is better revealed. The image processing was conducted in “Gwyddion”, while “ImageJ” open-source software was employed for the image analysis.

The ionomers’ surfaces of the membrane samples showed morphologies with distinct phases. The ionic domains and hydrophobic backbones were identified following the procedure developed by James et al.[27]. Post treatment of the phase images permitted to characterize the different domains. After fixing the phase scale between  $-10^\circ$  and  $10^\circ$ , a tailored procedure, which automatically iterates a threshold, a binarization, a noise correction, a watershed segmentation, and a particle analysis, furnished the proportion of surface of ionic domains and their average size. Five images for each polymer were analyzed.

#### 2.4.6. Organic flow battery single cell tests

##### 2.4.6.1. Charge-discharge cycling

The cell tests were carried out in an air-conditioned room ( $22^\circ\text{C}$ ). All membranes were investigated in a standard lab-scale flow battery single cell with an active area of  $5\text{ cm}^2$  (JenaBatteries GmbH), which was reported previously [15,20,28]. The cell setup adopts a sandwiched architecture with a ‘flow-through’ design of flow field. 10 mL of  $1.12\text{ mol}\cdot\text{L}^{-1}$  TMA-TEMPO aqueous solution (aq.) serves as the catholyte and 10 mL of  $1.49\text{ mol}\cdot\text{L}^{-1}$  MV (aq.) as the anolyte. Because the electrolyte conductivity is adequate for a working cell, no additional supporting electrolyte was added. The electrodes (thickness 4.6 mm), made of carbon felt, were used as received from the supplier (SGL Carbon, GFA6) and cut to designated size of  $5\text{ cm}^2$  square. A current collector (thickness 3 mm) made of graphite, type JP 945 (Mersen, France), was used. Ratio of N/P capacities was 1.33.

All membranes were firstly shaped into a square of  $3 \times 3\text{ cm}$  and then immersed in  $0.5\text{ M NaCl}$  (aq.) for at least 24 h before test. The cell setup was assembled with a sealing torque of  $1.5\text{ N}\cdot\text{m}$ . Afterwards, a gas leakage test was performed before connecting the reservoirs to the cell setup. The peristaltic pump (Heidolph Pumpdrive 5201, MASTERFLEX pump) speed was set at 80 rpm, which corresponds to  $16\text{ mL}\cdot\text{min}^{-1}$  as calibrated with the electrolyte solutions. A potentiostat/galvanostat with electrochemical impedance spectroscopy capability (Biologic VMP3, France) was used for all electrochemical experiments.

The cell resistance was measured *via* potentiostatic electrochemical impedance spectroscopy (PEIS) before the start of charge-discharge cycling tests and after it ended. The membrane resistance is calculated as the difference of cell resistance with membrane and without membrane.

A straightforward protocol was used for battery cycling that helps to differentiate the influence of resistance and crossover on capacity. The first charge-discharge cycle was carried out at low current density ( $20 \text{ mA}\cdot\text{cm}^{-2}$ ) to prime the cell and establish its initial capacity. Then the cell was charged-discharged continuously for 100 cycles at high current density ( $80 \text{ mA}\cdot\text{cm}^{-2}$ ). The last two cycles were operated at  $20 \text{ mA}\cdot\text{cm}^{-2}$  to provide evidence for a comprehensive assessment of the membrane performance. 1.5 V were used as upper cut-off voltage and 0.9 V as lower cut-off voltage. The coulombic efficiency (CE) and voltage efficiency (VE) were provided by EC-Lab Version 11.27, whereas energy efficiency (EE) is calculated from VE and CE. They are defined as:

$$CE = \frac{Q_d}{Q_c} \times 100\% \quad (6)$$

$$VE = \frac{U_d}{U_c} \times 100\% \quad (7)$$

$$EE = CE \times VE \quad (8)$$

Where  $Q_d$  is the discharging capacity,  $Q_c$  is the charging capacity at constant current;  $U_d$  is the mean discharging cell voltage and  $U_c$  is the mean charging cell voltage at constant current.

#### 2.4.6.2. Polarization curves

The polarization curve measurements were carried out after the charge-discharge cycling process mentioned above. Therefore, the cell was equipped with fresh electrolyte solutions to prevent influence from previous cross-contamination effects of redox-active molecules. Ten charge-discharge cycles were performed utilizing the same protocol as described above to prime the cell. Finally, the polarization curves were acquired at a flow rate of  $16 \text{ mL}\cdot\text{min}^{-1}$  by discharging at full state of charge (SOC) for 30 s over a range of current densities ( $10$  to  $600 \text{ mA}\cdot\text{cm}^{-2}$ ) until the cut-off voltage (0.2 V) was achieved. In-between the discharging steps, the cell was recharged at  $50 \text{ mA}\cdot\text{cm}^{-2}$  until the cut-off voltage of 1.5 V was reached. Afterwards, the pump speed was increased to 120 rpm, which corresponds to  $24 \text{ mL}\cdot\text{min}^{-1}$  by calibration, followed by the same process as at  $16 \text{ mL}\cdot\text{min}^{-1}$ . The discharging cell voltage of each cycle at the 30<sup>th</sup> second was taken to calculate the power density at the current density of this specific cycle.

### 2.4.6.3. Cyclic voltammetry

The electrolyte solutions in both reservoirs before and after the cell cycling tests were investigated via cyclic voltammetry in order to study crossover of TMA-TEMPO and MV. 100  $\mu\text{L}$  of the electrolyte sample was added into the 4.6 mL of 0.5 M NaCl (aq.) under the protection of argon after recording the background signal. The test setup is a three-electrode system, where glassy carbon serves as the working electrode, platinum wire as the counter electrode and silver/silver chloride as the reference electrode. Before each measurement, the glassy carbon electrode was polished with figure-eight motions in a water/alumina slurry to generate fresh surface [29]. Each electrolyte sample was scanned six times within the voltage range of 0.75 to 1.05 V at a scan rate of  $200 \text{ mV}\cdot\text{s}^{-1}$ . After each measurement, the background signal was subtracted and the fourth scan was chosen to prepare comparative graphs.

## 3. Results and discussion

### 3.1. Polymers and membranes preparation

Eight AEMs based on PPO-Br and PPO-6CO-Br polymers were prepared according to Scheme 1. The successful bromination of PPO in the benzylic position (PPO-Br) was confirmed by analysis of  $^1\text{H}$  NMR spectra [24] (Figure 1). The calculated degree of bromination was 26%, determined from the integrals of the characteristic proton peak of  $-\text{CH}_2\text{Br}$  at 4.3 ppm (Figure 1b, peak b) and the non-brominated  $\text{CH}_3$  groups (Figure 1b, peak a). The functionalization of PPO with bromohexanone (C6 spacer) using 6-bromo-1-hexanoyl chloride as a Friedel–Crafts acylation reagent was also determined by  $^1\text{H}$  NMR spectra [22,23] (Figure 1c). Specifically, the signal at 3 ppm (peak i) represents the protons adjacent to the ketone group. Whereas, the protons in the bromomethyl group are assigned to the signal at 3.4 ppm (peak e). The degree of functionalization was found to be 33%. Similarly, the degree of functionalization with 57 and 15% were obtained.

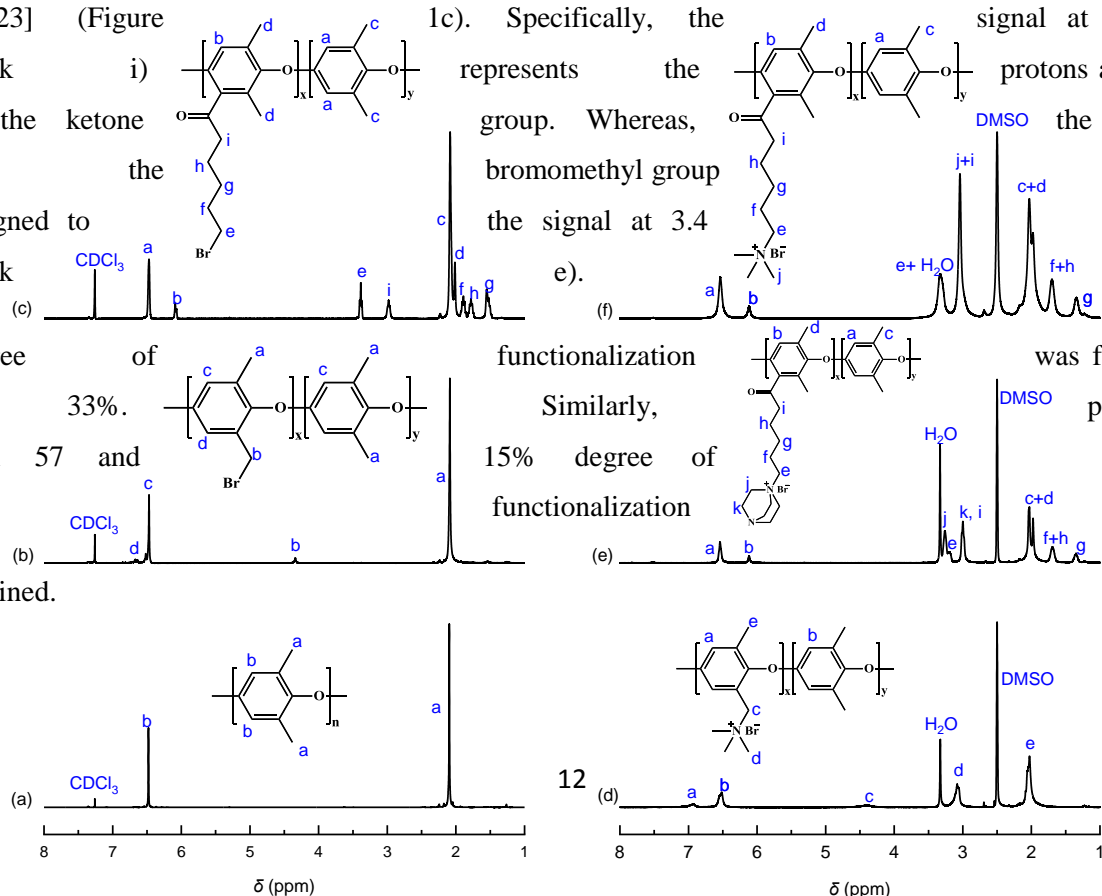


Figure 1:  $^1\text{H}$  NMR spectra (400 MHz,  $\text{CDCl}_3$ ) of (a) PPO, (b) PPO-Br ( $x = 0.26$ ) and (c) PPO-6CO-Br ( $x = 0.33$ ) polymers and membranes: (d) M8 ( $x = 0.26$ ), (e) M4 ( $x = 0.33$ ) and (f) M7 ( $x = 0.33$ ).

The bromination reaction was followed by quaternization with DABCO or TMA yielding cationic polymers. The quantitative substitution of the bromine units by the quaternary ammonium groups and formation of the desired product was confirmed by the  $^1\text{H}$  NMR for the non-cross-linked membranes (M3-M8). The  $^1\text{H}$  NMR spectra of M4, M7 and M8 in  $\text{Br}^-$  form are shown in Figure 1 (d,e and f) as representative examples of the membranes. In the case of M8 and M7, signals corresponding to the methyl protons of the  $-\text{N}^+(\text{CH}_3)_3$  groups appeared and correspond to peak d (Figure 1d) and j (Figure 1f), respectively. Similarly, the substitution of the Br units by DABCO in the case of M4 was confirmed by  $^1\text{H}$  NMR spectroscopy (Figure 1e). The characteristic signals corresponding to DABCO appeared at 3.27 (peak j) and 2.99 ppm (peak k). The NMR spectra of M5 is shown in Figure S2.

### 3.2. Membrane *ex-situ* characterization

All eight self-standing AEMs in  $\text{Cl}^-$  form were characterized in terms of thickness, IEC, water uptake and ion conductivity (Table 2). The values of IEC determined by titration were very close to those calculated from  $^1\text{H}$  NMR spectra, confirming the full quaternization of brominated PPO polymer precursors.

In particular, water uptake is a key factor as it affects the ionic conductivity, the dimensional stability and selectivity (cross contamination of redox active species) of the membranes [18]. At the same time, an optimum water uptake plays a significant role in formation of phase separated and percolated conducting domains and enhances the ionic conductivity of the membrane [30]. In general, increasing the IEC leads to increased water uptake and, hence, membrane ion conductivity and ionic domain sizes. For RFBs, a proper range of IEC is necessary to reach a balance between the membrane ion selectivity and conductivity [20].

Table 2 : Membranes *ex-situ* characterizations : Thickness, IEC, water uptake and Cl<sup>-</sup> ion conductivity

Membrane	Thickness ( $\mu\text{m}$ )	IEC ( $\text{mmol Cl}^- \cdot \text{g}^{-1}$ )		Water uptake (wt. %)	Cl <sup>-</sup> conductivity ( $\text{mS} \cdot \text{cm}^{-1}$ )	Hydration number ( $\lambda$ )
		<sup>1</sup> H NMR*	Titration			
M1	82	2.50**	$2.48 \pm 0.06$	8	1	1.8
M2	28	2.49**	$2.48 \pm 0.06$	10	0.8	2.2
M3	130	1.65	$1.63 \pm 0.05$	64	6	22
M4	60	1.65	$1.64 \pm 0.05$	42	5	14
M5	60	3.05	$3.0 \pm 0.11$	95	30	17.6
M6	60	0.96	$0.95 \pm 0.09$	19	3	11
M7	60	1.8	$1.79 \pm 0.06$	25	4.3	8
M8	60	1.8	$1.8 \pm 0.04$	20	2.1	6
FAA-3-50	50	1.6 - 2.1***	n.a.	17	1.7	5****

\* The IECs (which are determined using <sup>1</sup>H NMR) have a 5% margin of error.

\*\* Based on the degree of polymer bromination.

\*\*\* Data taken from the technical datasheet provided by the manufacturer.

\*\*\*\* The hydration number is calculated using the average value of the IEC range (1.6 ~ 2.1), which is 1.85 mmol Cl<sup>-</sup>·g<sup>-1</sup>.

The water uptake of the membranes also strongly depends on the degree of crosslinking. For instance, despite the high IECs ( $2.5 \text{ mmol Cl}^- \cdot \text{g}^{-1}$ ) of the M1 and M2 membranes, they exhibited extremely low water uptakes of 8 and 10 wt.%, respectively. As a result, the hydration numbers ( $\lambda$ ) were found to be only about 2. The theoretical degree of crosslinking of M1 and M2 membranes is estimated (equation 5) to be 31 and 12.5%, respectively. In comparison, the water uptakes of M4, M5, M6, which are non-cross-linked are much higher. The water uptakes of these membranes increased with the increase of IECs. Among them, M5 achieved as high as 95 wt.% water uptake owing to the high IEC of  $3.0 \text{ mmol Cl}^- \cdot \text{g}^{-1}$ , which stems from the full quaternization of the two amine units in DABCO. Whereas the membrane with the lowest IEC (M6,  $0.95 \text{ mmol Cl}^- \cdot \text{g}^{-1}$ ) displayed the lowest water uptake (19 wt.%). It is noteworthy that

M3 and M4 show the same chemical structure and IEC, but the water uptake of M3 is found to be higher than M4. This could be due to potential formation of free volumes during the elaboration process caused by the utilization of high amount of DABCO in excess (Table 1) that will be washed from the membrane. Indeed, the thickness might have influenced the homogeneity of the evaporation rate of the solvent during the drying process and the amount of residual solvent. As a result, the  $\lambda$  of M6, M4 and M5 was found to be 11, 14 and 17.6, respectively.

In contrast, the reference FAA-3-50 membrane, which is reported to be a PPO-based polymer [31,32], displayed a low water uptake (17 wt.%) and  $\lambda$  (5 water molecules per ionic function).

Two TMA-based membranes with the same IEC, M7 and M8, exhibited water uptake values of 25 and 20 wt.%, respectively, lower than the DABCO-based membranes (M3 and M4) despite of having slightly higher IEC. This suggests the cation type is another important factor to consider, when designing AEMs for RFBs. The slightly higher water uptake in the case of M7 could be due to the presence of a C6 side chain spacer that allow the increase of free volume as well as the formation of larger ionic domains which promote distinct water rich domains [33]. As a result, the  $\lambda$  of M7 (8 water molecules per ionic function) was higher than that of M8 (6 water molecules per ionic function).

Besides water uptake, a membrane with high  $\text{Cl}^-$  ion conductivity is important for having an AORFB with high power density. The  $\text{Cl}^-$  ion conductivity of the membranes, measured at room temperature, is summarized in Table 2. Among all the membranes, M5 recorded an outstanding  $\text{Cl}^-$  ion conductivity of  $30 \text{ mS}\cdot\text{cm}^{-1}$ . This high value could be attributed to the very high IEC (since both amine units of DABCO are quaternized) and water uptake of the membrane. However, the membrane was brittle, especially in dry form. The high-water uptake, that is inducing a high swelling degree, compromises the mechanical integrity of the membrane. In contrast, M1 and M2 show only about  $1 \text{ mS}\cdot\text{cm}^{-1}$   $\text{Cl}^-$  ion conductivity due to the crosslinked structure of the membranes. It constrains flexibility of the polymer chain, affecting (i) their water uptake capacities and (ii) the mobility of the ionic species [34]. In both membranes, only two water molecules can be taken up per ionic function, thereby reducing the ionic dissociation and the ability of the side chain to form percolated ionic clusters. As expected, the conductivities of M3, M4, M5 and M6 agree with their IEC and water uptake. The  $\text{Cl}^-$  ion conductivity of M7 doubled the value of M8 membrane. This could be due to the presence of a spacer in the former membrane, which promotes hydrophilic-hydrophobic nanophase separation [34–36] and, thus, the formation of more efficient and larger ionic conductive channels. AFM images of the surface and bulk morphologies of the M7 and M8 membranes were acquired to further study the phenomenon (Figure 2 and 3). The phase separation between the ionic and hydrophobic domains is clearly visible. The surface proportion of ionic domains is equal to 28% and 25% for M7 and M8, respectively, following the trend of water uptake values. This



difference is essentially reflected in an increase in the ionic domain area from 306 nm<sup>2</sup> (M8) to 358 nm<sup>2</sup> (M7) (Table S1). Both membranes reveal a bimodal size distribution of ionic domains with a first population of an average size of 50 nm<sup>2</sup> and the second one with an average size of 500 nm<sup>2</sup>. An increased proportion of the larger domain population corresponds to the increase in water uptake. A similar increase of ionic conductivity by introducing a spacer between a polymer backbone and cation has been reported elsewhere [23]. For comparison, the commercial reference membrane FAA-3-50 had a lower Cl<sup>-</sup> conductivity of only 1.7 mS·cm<sup>-1</sup> at room temperature, due to its low water uptake and IEC.

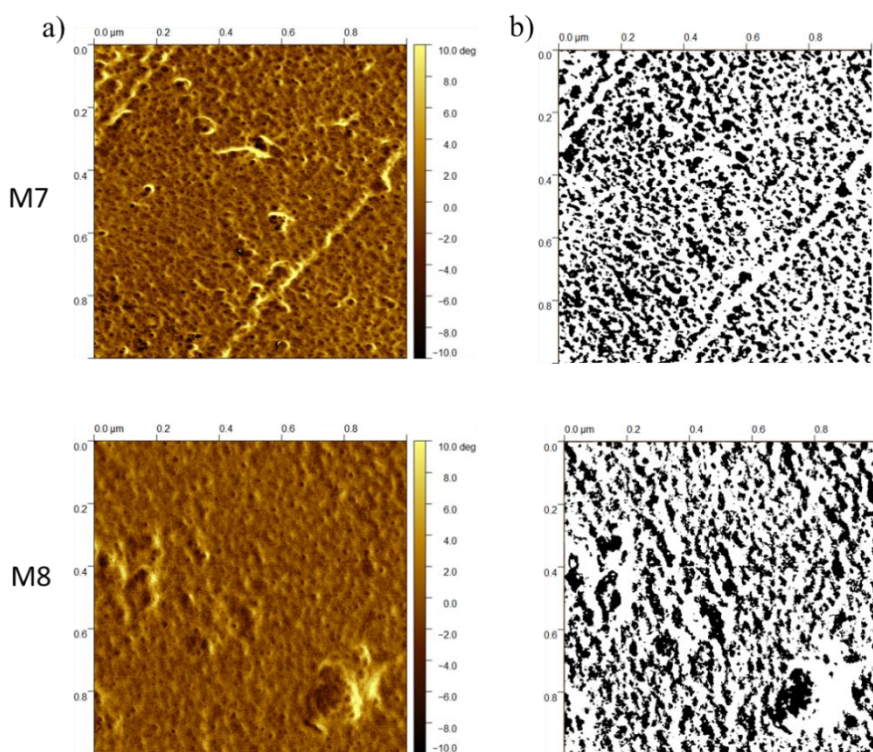


Figure 2: a) AFM phase images of M7 and M8 membranes (scan size 1 μm x 1 μm).; b) Post-treatment of AFM phase images (binarization). Darker regions correspond to the humidified ionic domains and lighter regions to the hydrophobic domains [37].

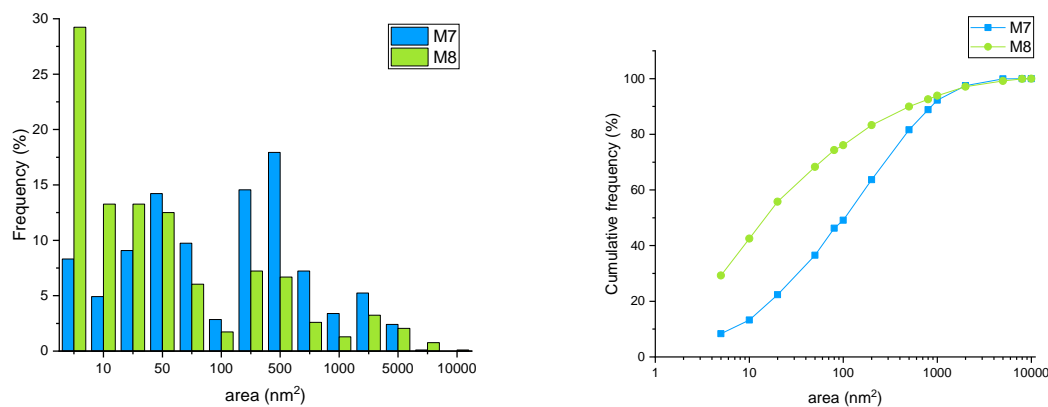


Figure 3: Area distribution of ionic domain for M7 and M8; left) frequency, right) cumulative frequency.

### 3.3. Battery performance

All membranes listed in Table 2, except M5 that was too brittle to be tested, were investigated in a TMA-TEMPO/MV based AORFB single flow battery cell. Tables S2 and S3 summarize the cell performance of the prepared AEMs and of the reference membrane FAA-3-50 characterized by initial capacity, capacity retention after long-term cycling, efficiencies (CE, VE, EE), resistance and peak power density; all of which are thoroughly discussed in the following sections.

#### 3.3.1. Membrane resistance

The resistance of the membranes was investigated in the TMA-TEMPO/MV based cell, both before and after the charge-discharge cycling test (Table 3). The results are in agreement with the membrane properties and structures (IEC, crosslinking/linear and thickness).

For instance, M1 and M2 displayed a rather high membrane resistance because of their low conductivity, which is assigned to their cross-linked structures. Despite having a similar IEC, M3 showed a higher resistance than M4 due to its larger thickness, but the ratio is lower than 2 (thickness ratio: 2.1), suggesting that the M3 membrane polymer is more conductive than M4. Surprisingly, M6 revealed almost the same resistance before cycling as M4 despite its much lower conductivity and a similar thickness. Notwithstanding the similarity of the two membrane resistances before cycling, the resistance of M6 was higher by more than 30% than that of M4 after the cycling process and hence, corresponds to the IEC and Cl<sup>-</sup> ion conductivity value. This effect is attributed to the different swelling behavior/speed of the membranes over the cycling process, stemming from a different extent of functionalization being present in both membranes (15% vs. 33%).

M7 displayed much lower resistance with respect to M8, being well in line with the *ex-situ* ionic conductivity. The effect is facilitated by the C6 spacer and its positive influence on membrane morphology and water uptake. Moreover, with similar IEC but much higher chloride ion conductivity than the reference membrane, M7 exhibited the same membrane resistance as FAA-3-50.

Table 3: In-situ membrane resistance acquired in the TMA-TEMPO/MV based AORFB single cell system (5 cm<sup>2</sup> active area).

Membrane	Membrane resistance/ $\Omega$	
	Before cell test	After cell test
M1	1.44	1.41
M2	1.09	1.37
M3	0.44	0.36
M4	0.28	0.26
M6	0.28	0.34
M7	0.26	0.28
M8	0.53	0.58
FAA-3-50	0.26	0.30

### 3.3.2. Capacity retention

The capacity accessible at high currents (*i.e.*, power capability at high over potentials) and the capacity retention/fade of a flow battery cell over long-term operation indicate the capability of the system to deploy energy, the compatibility of the redox-active materials and the membrane as well as the stability of both. Being two key components in a flow battery system, redox-active molecules and membranes, contribute equally to the accessible capacity and capacity retention. The long-term cycling stability of TMA-TEMPO and MV-based AORFB system has already been evidenced at concentration of 2 M in aqueous solution [15], providing a steady system for assessing and comparing the cell performance of the prepared AEMs.

The discharge capacities as a function of the cycle number for all tested membranes are shown in Figure 4. Membranes M1 and M2 reveal a relatively low accessible capacity at high current density (80 mA·cm<sup>-2</sup>). This effect is a result of the high membrane resistance (Table 3), *i.e.*, low Cl<sup>-</sup> ion conductivity, which causes high over potential resulting from ohmic resistance. Since the resistance is influenced by temperature, small day-to-night temperature changes (<2 K) in room temperature have a strong impact on the cell performance, causing a waving capacity curve, especially when the resistance is high. Both membranes share a similar trend in capacity fade, yet have different causes as indicated by resistance measurements and cyclic voltammograms (CV) acquired of the electrolyte solutions taken from the

anolyte and catholyte compartments after the cycling experiments. The CV for M2 suggests only minor cross-contamination of TMA-TEMPO and MV. Therefore, the speed-up decay in accessible capacity of the cell after 30<sup>th</sup> cycle stems from the increasing membrane resistance from 1.09  $\Omega$  to 1.37  $\Omega$  (Table 3), because higher overpotential will make the cell reach the cutoff voltage earlier, thus a lower share of the theoretical capacity is accessed. For the cell employing M1, the membrane resistance did not change considerably and no crossover of TMA-TEMPO/MV was observed (Figure S3 (A) and (B)). This cell test was aborted because a gradual external leakage occurred from 40<sup>th</sup> cycle and not repeated due to the poor overall performance.

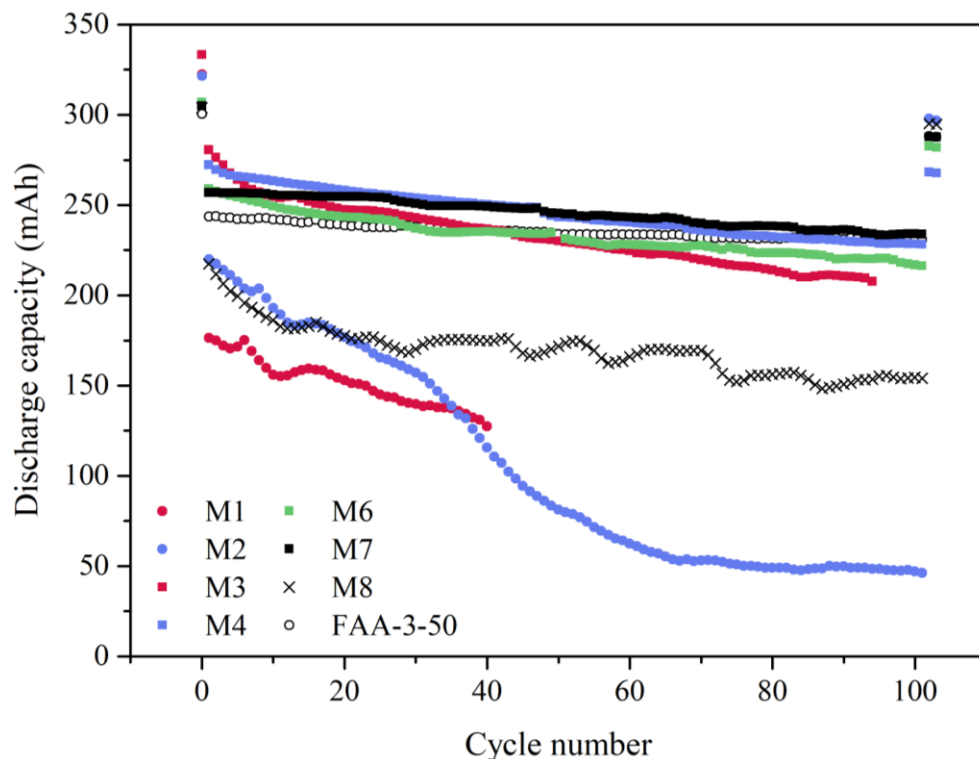


Figure 4: Discharge capacities of the TMA-TEMPO/MV based single cells using the series of prepared AEMs and the reference membrane FAA-3-50 over cycle number at different current densities.

The low cycling performance of the crosslinked membranes, M1 and M2, were attributed to their low ionic conductivity nature, so membrane M3 based on linear polymers was investigated. M3 exhibits higher performance due to its lower internal resistance (Figure 4, Table S2); however, M3 shows high capacity fade upon long-term cycling (26%) and small crossover of MV and TMA-TEMPO. After disassembling the test cells, the active area of M3 was observed to be colored brown, whereas M1 and M2 exhibited minor or no color change (Figure S4). The color change is probably attributed to the irreversible oxidation of the free tertiary amine groups of DABCO in M3 caused by the interaction with nitroxyl radical TMA-TEMPO [38–40]. Using <sup>1</sup>H NMR and ATR-FTIR spectroscopy (Figure S5), the chemical

structure of the membrane before and after cycling was analyzed. Since no changes were apparent it is safe to assume that the reaction is limited and the amount of amine modification is too small after 100 cycles to be detected by such analysis. Both highly cross-linked membranes M1 and M2 have very low water uptakes as well as lower amount of free amine groups and are, therefore, less exposed to the oxidation reaction. M4 displayed an outstanding capacity retention of 84% after 100 cycles at  $80 \text{ mA cm}^{-2}$ , whereas M3 exhibited only 74%, partly because of the slightly higher membrane resistance (Table S2).

Three membrane synthesis strategies were introduced to avoid the aging process and/or capacity fade: (i) M5 in which both tertiary amines were fully quaternized, (ii) M6 with lower IEC in order to decrease its water uptake and (iii) M7 with TMA replacing DABCO. In the case of M6 membrane, the lower degree of functionalization of the polymer backbone results in less free tertiary amine groups exposed to TMA-TEMPO oxidation, as well as lower water uptake and possibly lower TMA-TEMPO penetration, which can interact with tertiary amine. Meanwhile, the good chloride ion conductivity and low water uptake of M6 guarantee its low membrane resistance (Table 3) and high TMA-TEMPO/MV retention i.e., no cross-contamination (Figure S3(C) and (D)). Therefore, a high capacity retention (83%) at the current density of  $80 \text{ mA}\cdot\text{cm}^{-2}$  was observed for M6. It should be noted that this value is very close to the value obtained for M4, but the capacity retention at  $20 \text{ mA}\cdot\text{cm}^{-2}$  was increased by 5%. Therefore, lowering the IEC resulted in an improvement on the capacity retention. However, this comes at the cost of power capability, as can be seen from smaller values for the accessible capacity at high current density of  $80 \text{ mA}\cdot\text{cm}^{-2}$  and peak power density (Table S3).

As for M7, when DABCO is replaced by TMA, the ionic group is no longer subjected to oxidation catalyzed by the nitroxyl radical. At the same time, the high ionic conductivity of M7 resulted in low membrane resistance whereas its low water uptake maintains the selectivity for  $\text{Cl}^-$  ion. Therefore, the capacity and capacity retention of the cell with M7 at both low and high current densities preserved at a high level. A capacity retention of 99.94%/cycle at  $20 \text{ mA}\cdot\text{cm}^{-2}$  (capacity retention of 94% at the 103<sup>rd</sup> cycle) was recorded, which is a very promising result. Similarly, the commercial membrane FAA-3-50 also achieved high-level capacity retention at both current densities. As shown in Table S2, a capacity retention of 95% at  $20 \text{ mA}\cdot\text{cm}^{-2}$  was observed. As the exact polymer structure of FAA-3-50 is not publicly disclosed, it is hard to identify the root cause of the difference, not to mention the complex nature of the microstructures of membranes.

With similar membrane properties as FAA-3-50, M8 exhibited a higher capacity retention (97%) at  $20 \text{ mA}\cdot\text{cm}^{-2}$ . However, removing the C6 spacer while keeping the TMA moiety in M8 resulted in a higher membrane resistance and, thereby, higher over potentials. Consequently, the low ionic conductivity made it difficult to access the full capacity at a higher current density ( $80 \text{ mA}\cdot\text{cm}^{-2}$ ), only 71% of the capacity

was available. The regular fluctuation in capacity is assigned to the waving room temperature during summertime, as confirmed in an independent experiment with FAA-3-50 (Figure S6). Figure S2 (E and F) shows the CVs of the electrolyte solutions of the test cell using FAA-3-50 and M8 membranes. As a representative example, the charge-discharge curve of 1<sup>st</sup> and last cycle of M7 membrane at 80 mA·cm<sup>-2</sup> is provided in Figure S7.

In summary, the best results for the TMA-TEMP/MV flow battery can be achieved, when preventing membrane aging by avoiding the presence of free amine groups and introducing a spacer to promote the formation of phase separated ionic clusters. Capacity retention correlates strongly with the water uptake and Cl<sup>-</sup> ion conductivity, suggesting aiming at a high-performance membrane which possess a high conductivity and sufficiently low water uptake.

### 3.3.3. Coulombic efficiency, voltage efficiency and energy efficiency

Coulombic efficiency (CE) indicates the degree of cross-contamination, which directly relates to the membrane ion selectivity. Voltage efficiency (VE), expressed as mean discharging cell voltage divided by mean charging cell voltage at constant current, reflects the over potentials and resistance level of the system, which is strongly determined by the membrane resistance. As shown in Figure 5, all tested membranes exhibited excellent CE of over 99.3%, indicating a high membrane selectivity of chloride ion, which was further confirmed by the cyclic voltammograms of the electrolyte solutions taken from the test cell after the charge-discharge cycling tests (Figure S3).

As the CEs are almost identical for all the membranes (close to 100%), the voltage efficiencies (VEs) and energy efficiencies (EE) are close and mainly associated with the internal resistance, which in turn is dominated by the membrane resistance. The VEs of the cells with M1, M2, M3 and M8 were reduced to different extent varying with the membrane resistance (Table 3). M6 has a similar membrane resistance as FAA-3-50, resulting in similar voltage efficiency. With slightly lower membrane resistance than FAA-3-50, M4 and M7 displayed a bit higher voltage efficiency (80%) at 80 mA·cm<sup>-2</sup>. Therefore, the energy efficiency was enhanced to a certain level by further lowering the membrane resistance without sacrificing the membrane ion selectivity.

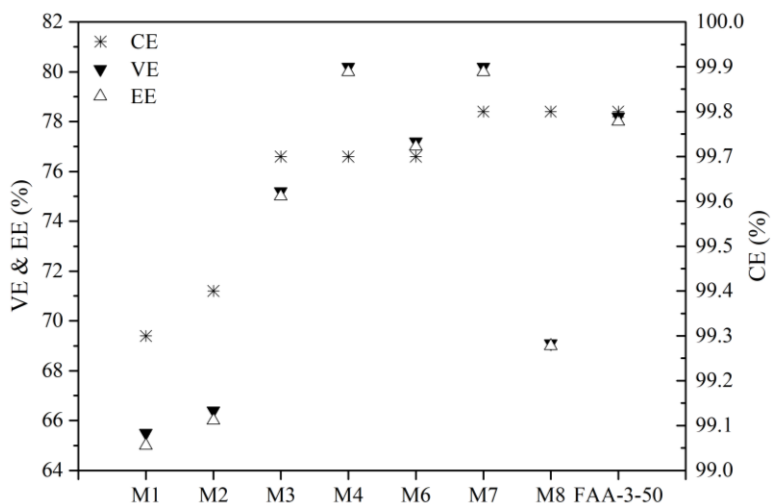


Figure 5: Average coulombic efficiency (CE), voltage efficiency (VE) and energy efficiency (EE) of 100 consecutive charge-discharge cycles at a constant current density of  $80 \text{ mA}\cdot\text{cm}^{-2}$  in TMA-TEMPO/MV based single cells with the series of prepared AEMs and the reference membrane FAA-3-50.

### 3.3.4. Power density

Owing to their good battery performance, M3, M4, M6, M7, M8 and FAA-3-50 membranes were chosen for an in-depth study of their power capability. Therefore, polarization curves were acquired at two different flow rates ( $16$  and  $24 \text{ mL}\cdot\text{min}^{-1}$ ) after the cycling tests. Due to the optimization of the system, the polarization behaviour is dominated by the resistance of the membrane. Other limitations associated with redox reaction and mass transport limitation are minor in the range of the current density investigated.

As can be seen from Figure 6, the peak power densities of M3, M4, M6 and M7 were improved comparing to the reference membrane. Within the expectation, the peak power density of the tested membranes has a reverse relation to the corresponding membrane resistance (Table S3), except for M3, whose power density was probably influenced by the aging process upon interaction with the TMA-TEMPO redox couple. In a way to uncover the power density undisturbed from aging, the polarization curve of a freshly prepared M3 was recorded using fresh electrolytes. The peak power density of the cell with pristine M3 turned out to be  $376 \text{ mW}\cdot\text{cm}^{-2}$  at flow rate of  $16 \text{ mL}\cdot\text{min}^{-1}$ , promoted by 60% comparing to that of FAA-3-50 (Figure 6), whereas, the aged M3 displayed a peak power density of only  $269 \text{ mW}\cdot\text{cm}^{-2}$  (Table S3).

With respect to the other membranes, the peak power densities were found to be in agreement with their ion conductivities, *i.e.*, cell resistances, since the membranes have same thickness. Accordingly, M4, M7,

M6 and M8 delivered a maximum power density of 316, 293, 284 and 183  $\text{mW}\cdot\text{cm}^{-2}$ , respectively, at a flow rate of  $16\text{ mL}\cdot\text{min}^{-1}$ . The peak power density of the cell with FAA-3-50 ( $235\text{ mW}\cdot\text{cm}^{-2}$ ) is between that of M8 and M3 (aged), thus several of our membranes present better performances. The I-V curves are shown in Figure S8.

Finally, the influence of battery operating conditions was simulated by variation of the electrolyte flow. An increased mass transport is supposed to counteract the depletion of TMA-TEMPO and MV during the redox reaction. By increasing the flow rate from  $16$  to  $24\text{ mL}\cdot\text{min}^{-1}$ , the peak power density of all tested membranes was raised by 1.4 to 4.7% (Figure S9).

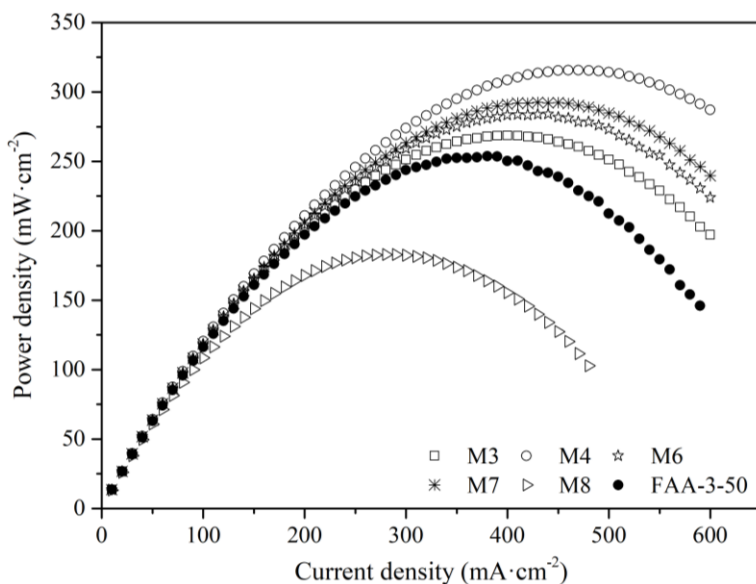


Figure 6: Power densities of the cells with membranes M3, M4, M6, M7, M8 and FAA-3-50 over different current densities at the flow rate of  $16\text{ mL}\cdot\text{min}^{-1}$  after the cycling tests.

Intended for practical application, we compared the highest peak power density value achieved in this work to those reported in different flow battery systems, including the conventional vanadium system, semi-organic systems and all-organic systems (Table S4). Technically, power density is determined by the cell voltage and the cell resistance including over potentials. Therefore, any factor in a battery that makes a difference to those two parameters can ultimately change the acquired power density. As complex methods and systems were involved in the literature, a comparison under the same condition is beyond possibility. Nevertheless, it allows to assess the power capability achieved in this work for its practicability. To the best of our knowledge, the power density achieved with membranes M3 to M7 is superior to the reported all-organic flow systems.



Comparing outside all-organic systems, the peak power density of  $388 \text{ mW}\cdot\text{cm}^{-2}$  in TMA-TEMPO/MV with M3 ranks in the middle in the listed systems. The main reason lies in the different nature of the membrane, the supporting electrolyte and flow rate. While the system described above uses AEM and chloride ions, the literature examples employ highly conductive, but corrosive acid-based solutions (*e.g.*,  $\text{H}_2\text{SO}_4$ ) and cation exchange membranes. Hence, the results are within expectation and demonstrate that milder electrolyte solutions in combination with optimized membranes have become suitable for practical application.

Looking into detail, the extra high power density of  $2,780 \text{ mW}\cdot\text{cm}^{-2}$  of VRFB system involved accumulated efforts on optimizing the flow field, electrode material, flow rate and membrane [41]. Similarly, in the semi-organic system employing 2,7-(anthraquinone-2,6-disulfonate) AQDS/ $\text{Br}_2$ , a peak power density of  $1,000 \text{ mW}\cdot\text{cm}^{-2}$  was achieved in an optimized condition of electrolyte composition, electrode, membrane, flow rate and temperature. For instance, when the flow rate of VRFB system increased from 20 to  $50 \text{ mL}\cdot\text{min}^{-1}$ , the mass and ion transport was distinctly enhanced, which also significantly contributes to the ultimate power density [41]. By increasing from room temperature to  $40 \text{ }^\circ\text{C}$ , the peak power density of the semi-organic system 2,7-AQDS $\text{Na}_2$ / $\text{Br}_2$  could be elevated from 400 to  $450 \text{ mW}\cdot\text{cm}^{-2}$  [42]. In comparison, the peak power density achieved in this work is simply based on optimized membrane; other aforementioned parameters are beyond the scope of this work. Therefore, the authors are convinced that by further optimization of electrode, electrolyte composition, flow field design, flow rate and temperature, higher power density in TMA-TEMPO/MV based AORFB can be reached using the membranes presented here.

### 3.4. Membrane property-battery performance interrelation

Based on those results, we summarize the membrane property-performance interrelation in a net graph as shown in Figure 7. In this work, all tested membranes displayed high coulombic efficiency of over 99% and only slight or no crossover, which relies on low water uptake (below 64 wt.%). Therefore, the energy efficiency is mainly dependent on the voltage efficiency, which relates directly to the membrane resistance as the redox-active molecules are defined. This influence becomes more apparent when the membrane resistance is high. For example, membrane resistance of M8 is  $0.528 \text{ }\Omega$ , its energy efficiency at  $80 \text{ mA}\cdot\text{cm}^{-2}$  is 69%. In contrast, the membrane resistance of M3 is  $0.437 \text{ }\Omega$ , its energy efficiency at the same current density increases to 75%. When the membrane resistance decreases to  $0.257 \text{ }\Omega$  (M7), the energy efficiency increases to 80% under the same condition. Because the resistance during the cycling process fluctuates within a certain range, the energy efficiency over long-term cycling may not follow the trend for low-resistance membranes. Another parameter that is strongly influenced by membrane resistance is the peak power density. As discussed in previous sections, the peak power density will

increase with decreasing membrane resistance in general cases. However, potential membrane aging can alter the mass transport process, thus affecting the peak power density.

The third parameter, capacity retention, generally depends on both the membrane resistance and membrane perm-selectivity. Membrane resistance is found to be related to thickness, ion conductivity and water uptake, yet does not follow simple rules. For instance, the thickness of M3 (130  $\mu\text{m}$ ) is twice that of M8 (60  $\mu\text{m}$ ), but the membrane resistance of M3 is distinctly lower than that of M8. In this case, the high ion conductivity of M3 compensates for its thickness while M8 compromises to its low ion conductivity due to the lack of 6C spacer to the polymer backbone. The commercial membrane FAA-3-50 is reported to bear no spacer as well, its ion conductivity and water uptake are similar (slightly lower) to that of M8. However, its membrane resistance is much reduced comparing to M8, probably stemming from its higher IEC or the cation type. This addresses the importance to understand the structure-property-performance relationship based on defined polymer structures.

Hence, when designing an ion exchange membrane for AORFB, low water uptake and high ionic conductivity are targeted. Therefore, a membrane with moderate IEC is required and its value has to be modulated as function of polymer structure. Thus, when no carbon spacer is included between the rigid polymer backbone and the cation, higher IEC is required to overcome poor ionic cluster organization and achieve a membrane with sufficient ionic conductivity and low resistance. When a flexible spacer, such as 6 C is included, it is important to control the water uptake at an acceptable level where only slight or no crossover of redox-active molecules is allowed. Because polymer crosslinking has a significant impact on chain mobility, ionic cluster structure and water uptake, a high IEC is required to provide a sufficient ion conductivity. To ensure long-term stability, the chosen polymer backbone and ionic type should possess chemical stability and mechanical strength to avoid potential aging and/or degradation. Following these strategies, good battery performance is in anticipation.

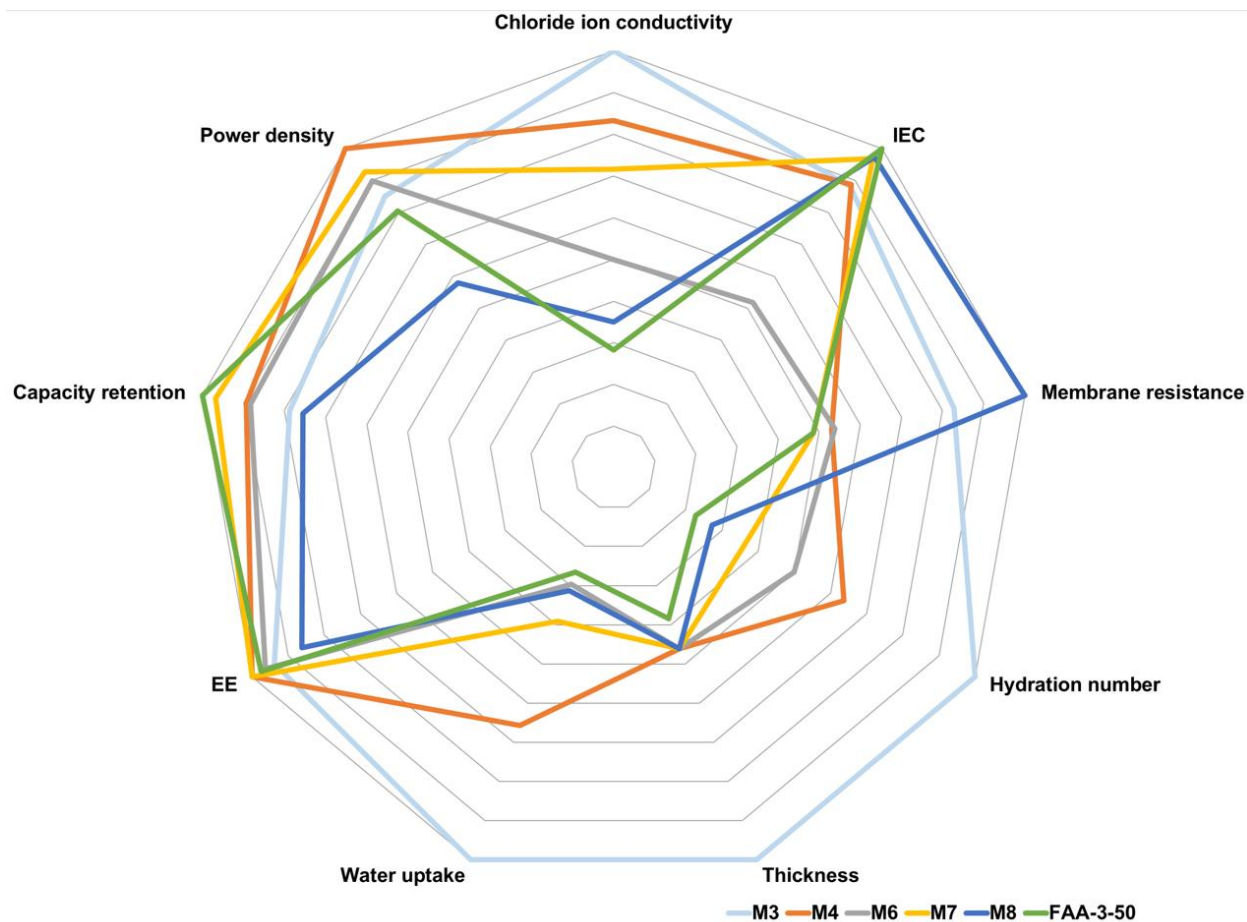


Figure 7: Overview of membrane property-battery performance interrelation. All data are normalized according to the highest values. Membrane resistance before cycling experiment is used.

## 4. Conclusion

A series of eight anion exchange membranes based on poly(p-phenylene oxide) backbone varying in the degree of functionalization, cation type and polymer architecture were prepared, followed by *ex-situ* membrane characterizations featuring IEC, water uptake and chloride ion conductivity. Membrane M5, bearing fully quaternized DABCO groups, a linear polymer architecture and showing a high chloride ion conductivity of  $30 \text{ mS}\cdot\text{cm}^{-1}$ , turned out to be brittle and its mechanical strength is expected to be compromised by its swelling degree. All other membranes were mechanically stable and, hence, subsequently investigated in a TMA-TEMPO/methyl viologen based redox flow battery test cell to probe how the cell performance is manipulated by polymer structure and the corresponding membrane properties. Despite the absence of crossover of redox species, the partially DABCO-crosslinked M1 and M2 membranes, exhibited fast capacity fades upon battery cycling and low energy efficiencies due to their high cell resistance. Whereas, the DABCO-based linear polymer membrane showed capacity fade

following a permanent coloration and aging of the membranes. This effect is attributed to a possible oxidation of the tertiary amine of M3 by the nitroxyl radical TMA-TEMPO, which is a renowned oxidation catalyst. However, the M3 membrane displayed a high chloride ion conductivity ( $6 \text{ mS}\cdot\text{cm}^{-1}$  at room temperature) and freshly prepared membranes reveal a peak power density of  $376 \text{ mW}\cdot\text{cm}^{-2}$  that is extensively promoted by 60% as compared to the commercial reference membrane FAA-3-50 ( $235 \text{ mW}\cdot\text{cm}^{-2}$ ). When the aging is lowered or avoided by either lowering the degree of functionalization or replacing the DABCO cation with a trimethylammonium moiety, the resulting membranes M6 and M7 exhibited improved performance in capacity retention, energy efficiency as well as peak power density. Overall, the M7 membrane-cell, that is using a linear polymer structure and a fully quaternized trimethylammonium cation as ion exchange group attached *via* a C6 spacer, achieved the best overall cell performance. It showed appreciable high capacity retention (94% after over 100 consecutive cycles) and delivered higher peak power density ( $293 \text{ mW}\cdot\text{cm}^{-2}$  at  $16 \text{ mL}\cdot\text{min}^{-1}$ ) and energy efficiency (80%) than the FAA-3-50. In addition, the production cost of M7 is estimated to be low (Table S5). These results will greatly contribute to the future market of ORFBs with competing low cost and high performance. In future studies, we believe it is critical to investigate the long-term durability of the membranes in the AORFB cell, permeability rates of active species across the membranes, swelling ratios and tensile strengths of the membranes.

### **Competing interests:**

The authors have no competing interests to declare.

### **Author contribution:**

**Misgina Tilahun Tsehaye** performed the synthesis and *ex-situ* characterizations of the membranes. **Xian Yang** performed the electrochemical measurements. **Misgina Tilahun Tsehaye:** conceptualization, methodology, investigation, writing- original draft preparation. **Xian Yang:** conceptualization, methodology, investigation, writing- original draft preparation. **Tobias Janoschka:** supervision, project administration, writing - review & editing. **Martin D. Hager:** supervision, writing - review & editing. **Ulrich S. Schubert:** supervision, writing - review & editing. **Emilie Planes:** analysis and writing of AFM part. **Fannie Alloin:** supervision, writing - review & editing. **Cristina Iojoiu:** supervision, project administration writing - review & editing.

**Funding:** This project has received funding from the European Union's Horizon 2020 research and innovation programme under the Marie Skłodowska-Curie Grant Agreement no. 765289.

## References

- [1] E. Sánchez-Díez, E. Ventosa, M. Guarnieri, A. Trovò, C. Flox, R. Marcilla, F. Soavi, P. Mazur, E. Aranzabe, R. Ferret, Redox flow batteries: Status and perspective towards sustainable stationary energy storage, *J. Power Sources*. 481 (2021) 228804. <https://doi.org/10.1016/j.jpowsour.2020.228804>.
- [2] A.Z. Weber, M.M. Mench, J.P. Meyers, P.N. Ross, J.T. Gostick, Q. Liu, Redox flow batteries: a review, *J. Appl. Electrochem.* 41 (2011) 1137–1164. <https://doi.org/10.1007/s10800-011-0348-2>.
- [3] G.L. Soloveichik, Flow batteries: Current status and trends, *Chem. Rev.* 115 (2015) 11533–11558. <https://doi.org/10.1021/cr500720t>.
- [4] P. Alotto, M. Guarnieri, F. Moro, Redox flow batteries for the storage of renewable energy: A review, *Renew. Sustain. Energy Rev.* 29 (2014) 325–335. <https://doi.org/10.1016/j.rser.2013.08.001>.
- [5] European Commission, The European Green Deal, *Eur. Comm.* 53 (2019) 24. <https://doi.org/10.1017/CBO9781107415324.004>.
- [6] J. Winsberg, T. Hagemann, T. Janoschka, M.D. Hager, U.S. Schubert, Redox- flow batteries: From metals to organic redox- active materials, *Angew. Chemie Int. Ed.* 56 (2017) 686–711. <https://doi.org/10.1002/anie.201604925>.
- [7] G. Kear, A.A. Shah, F.C. Walsh, Development of the all-vanadium redox flow battery for energy storage: a review of technological, financial and policy aspects, *Int. J. Energy Res.* 36 (2012) 1105–1120. <https://doi.org/10.1002/er.1863>.
- [8] X. Wei, W. Pan, W. Duan, A. Hollas, Z. Yang, B. Li, Z. Nie, J. Liu, D. Reed, W. Wang, V. Sprenkle, Materials and systems for organic redox flow batteries: Status and challenges, *ACS Energy Lett.* 2 (2017) 2187–2204. <https://doi.org/10.1021/acseenergylett.7b00650>.
- [9] K. Wedege, E. Dražević, D. Konya, A. Bientien, Organic redox species in aqueous flow batteries: Redox potentials, chemical stability and solubility, *Sci. Rep.* 6 (2016) 39101. <https://doi.org/10.1038/srep39101>.
- [10] B. Yang, L. Hooper-Burkhardt, F. Wang, G.K. Surya Prakash, S.R. Narayanan, An inexpensive aqueous flow battery for large-scale electrical energy storage based on water-soluble organic redox couples, *J. Electrochem. Soc.* 161 (2014) A1371–A1380. <https://doi.org/10.1149/2.1001409jes>.
- [11] B. Schwenzer, J. Zhang, S. Kim, L. Li, J. Liu, Z. Yang, Membrane development for vanadium redox flow batteries, *ChemSusChem.* 4 (2011) 1388–1406. <https://doi.org/10.1002/cssc.201100068>.
- [12] C. Minke, T. Turek, Economics of vanadium redox flow battery membranes, *J. Power Sources.* 286 (2015) 247–257. <https://doi.org/10.1016/j.jpowsour.2015.03.144>.
- [13] Y. Shi, C. Eze, B. Xiong, W. He, H. Zhang, T.M. Lim, A. Ukil, J. Zhao, Recent development of membrane for vanadium redox flow battery applications: A review, *Appl. Energy.* 238 (2019) 202–224. <https://doi.org/10.1016/j.apenergy.2018.12.087>.

- [14] Y.A. Hugo, W. Kout, F. Sikkema, Z. Borneman, K. Nijmeijer, In situ long-term membrane performance evaluation of hydrogen-bromine flow batteries, *J. Energy Storage*. 27 (2020) 101068. <https://doi.org/10.1016/j.est.2019.101068>.
- [15] T. Janoschka, N. Martin, M.D. Hager, U.S. Schubert, An Aqueous redox-flow battery with high capacity and power: The TEMPTMA/MV system, *Angew. Chemie Int. Ed.* 55 (2016) 14427–14430. <https://doi.org/10.1002/anie.201606472>.
- [16] K. Lin, Q. Chen, M.R. Gerhardt, L. Tong, S.B. Kim, L. Eisenach, A.W. Valle, D. Hardee, R.G. Gordon, M.J. Aziz, M.P. Marshak, Alkaline quinone flow battery, *Science* (80-. ). 349 (2015) 1529–1532. <https://doi.org/10.1126/science.aab3033>.
- [17] E.S. Beh, D. De Porcellinis, R.L. Gracia, K.T. Xia, R.G. Gordon, M.J. Aziz, A Neutral pH Aqueous Organic–Organometallic Redox Flow Battery with Extremely High Capacity Retention, *ACS Energy Lett.* 2 (2017) 639–644. <https://doi.org/10.1021/acsenenergylett.7b00019>.
- [18] L.J. Small, H.D. Pratt, T.M. Anderson, Crossover in membranes for aqueous soluble organic redox flow batteries, *J. Electrochem. Soc.* 166 (2019) A2536–A2542. <https://doi.org/10.1149/2.0681912jes>.
- [19] B. Hu, C. Seefeldt, C. DeBruler, T.L. Liu, Boosting the energy efficiency and power performance of neutral aqueous organic redox flow batteries, *J. Mater. Chem. A*. 5 (2017) 22137–22145. <https://doi.org/10.1039/C7TA06573F>.
- [20] M.T. Tsehaye, X. Yang, T. Janoschka, M.D. Hager, U.S. Schubert, F. Alloin, C. Iojoiu, Study of anion exchange membrane properties incorporating N-spirocyclic quaternary ammonium cations and aqueous organic redox flow battery performance, *Membranes (Basel)*. 11 (2021) 367. <https://doi.org/10.3390/membranes11050367>.
- [21] Y. Zhu, L. Ding, X. Liang, M.A. Shehzad, L. Wang, X. Ge, Y. He, L. Wu, J.R. Varcoe, T. Xu, Beneficial use of rotatable-spacer side-chains in alkaline anion exchange membranes for fuel cells, *Energy Environ. Sci.* 11 (2018) 3472–3479. <https://doi.org/10.1039/C8EE02071J>.
- [22] M.R. Hibbs, Alkaline stability of poly(phenylene)-based anion exchange membranes with various cations, *J. Polym. Sci. Part B Polym. Phys.* 51 (2013) 1736–1742. <https://doi.org/10.1002/polb.23149>.
- [23] J. Parrondo, M.J. Jung, Z. Wang, C.G. Arges, V. Ramani, Synthesis and alkaline stability of solubilized anion exchange membrane binders based on poly(phenylene oxide) functionalized with quaternary ammonium groups via a hexyl spacer, *J. Electrochem. Soc.* 162 (2015) F1236–F1242. <https://doi.org/10.1149/2.0891510jes>.
- [24] X. Tongwen, Y. Weihua, Fundamental studies of a new series of anion exchange membranes: Membrane preparation and characterization, *J. Memb. Sci.* 190 (2001) 159–166. [https://doi.org/10.1016/S0376-7388\(01\)00434-3](https://doi.org/10.1016/S0376-7388(01)00434-3).
- [25] H.W. Doughty, Mohr’s method for the determination of silver and halogens in other than neutral solutions, *J. Am. Chem. Soc.* 46 (1924) 2707–2709. <https://doi.org/10.1021/ja01677a014>.
- [26] A. Katzfuß, V. Gogel, L. Jörissen, J. Kerres, The application of covalently cross-linked BrPPO as AEM in alkaline DMFC, *J. Memb. Sci.* 425–426 (2013) 131–140. <https://doi.org/10.1016/j.memsci.2012.09.022>.
- [27] P.J. James, M. Antognozzi, J. Tamayo, T.J. McMaster, J.M. Newton, M.J. Miles, Interpretation of contrast in tapping mode AFM and shear force microscopy. A study of Nafion, *Langmuir*. (2001). <https://doi.org/10.1021/la000332h>.

- [28] T. Janoschka, N. Martin, U. Martin, C. Friebe, S. Morgenstern, H. Hiller, M.D. Hager, U.S. Schubert, An aqueous, polymer-based redox-flow battery using non-corrosive, safe, and low-cost materials, *Nature*. 527 (2015) 78–81. <https://doi.org/10.1038/nature15746>.
- [29] N. Elgrishi, K.J. Rountree, B.D. McCarthy, E.S. Rountree, T.T. Eisenhart, J.L. Dempsey, A Practical beginner's guide to cyclic voltammetry, *J. Chem. Educ.* 95 (2018) 197–206. <https://doi.org/10.1021/acs.jchemed.7b00361>.
- [30] Q. Duan, S. Ge, C.-Y. Wang, Water uptake, ionic conductivity and swelling properties of anion-exchange membrane, *J. Power Sources*. 243 (2013) 773–778. <https://doi.org/10.1016/j.jpowsour.2013.06.095>.
- [31] M.G. Marino, J.P. Melchior, A. Wohlfarth, K.D. Kreuer, Hydroxide, halide and water transport in a model anion exchange membrane, *J. Memb. Sci.* 464 (2014) 61–71. <https://doi.org/10.1016/j.memsci.2014.04.003>.
- [32] A.M. Barnes, B. Liu, S.K. Buratto, Humidity-dependent surface structure and hydroxide conductance of a model quaternary ammonium anion exchange membrane, *Langmuir*. 35 (2019) 14188–14193. <https://doi.org/10.1021/acs.langmuir.9b02160>.
- [33] H.-S. Dang, E.A. Weiber, P. Jannasch, Poly(phenylene oxide) functionalized with quaternary ammonium groups via flexible alkyl spacers for high-performance anion exchange membranes, *J. Mater. Chem. A*. 3 (2015) 5280–5284. <https://doi.org/10.1039/C5TA00350D>.
- [34] K. Yang, H. Ni, T. Shui, X. Chi, W. Chen, Q. Liu, J. Xu, Z. Wang, High conductivity and alkali-resistant stability of imidazole side chain crosslinked anion exchange membrane, *Polymer (Guildf)*. 211 (2020) 123085. <https://doi.org/10.1016/j.polymer.2020.123085>.
- [35] J. Liao, X. Yu, Q. Chen, X. Gao, H. Ruan, J. Shen, C. Gao, Monovalent anion selective anion-exchange membranes with imidazolium salt-terminated side-chains: Investigating the effect of hydrophobic alkyl spacer length, *J. Memb. Sci.* 599 (2020) 117818. <https://doi.org/10.1016/j.memsci.2020.117818>.
- [36] C.X. Lin, X.L. Huang, D. Guo, Q.G. Zhang, A.M. Zhu, M.L. Ye, Q.L. Liu, Side-chain-type anion exchange membranes bearing pendant quaternary ammonium groups via flexible spacers for fuel cells, *J. Mater. Chem. A*. 4 (2016) 13938–13948. <https://doi.org/10.1039/C6TA05090E>.
- [37] A.S. Badami, O. Lane, H.S. Lee, A. Roy, J.E. McGrath, Fundamental investigations of the effect of the linkage group on the behavior of hydrophilic-hydrophobic poly(arylene ether sulfone) multiblock copolymers for proton exchange membrane fuel cells, *J. Memb. Sci.* (2009). <https://doi.org/10.1016/j.memsci.2008.12.066>.
- [38] K. Sato, T. Ono, Y. Sasano, F. Sato, M. Kumano, K. Yoshida, T. Dairaku, Y. Iwabuchi, Y. Kashiwagi, Electrochemical oxidation of amines using a nitroxyl radical catalyst and the electroanalysis of lidocaine, *Catalysts*. 8 (2018) 649. <https://doi.org/10.3390/catal8120649>.
- [39] A.L. Bartelson, K.M. Lambert, J.M. Bobbitt, W.F. Bailey, Recent developments in the nitroxide-catalyzed oxidation of amines: Preparation of imines and nitriles, *ChemCatChem*. 8 (2016) 3421–3430. <https://doi.org/10.1002/cctc.201600858>.
- [40] M.F. Semmelhack, C.R. Schmid, Nitroxyl-mediated electro-oxidation of amines to nitriles and carbonyl compounds, *J. Am. Chem. Soc.* 105 (1983) 6732–6734. <https://doi.org/10.1021/ja00360a042>.
- [41] H.R. Jiang, J. Sun, L. Wei, M.C. Wu, W. Shyy, T.S. Zhao, A high power density and long cycle life vanadium redox flow battery, *Energy Storage Mater.* 24 (2020) 529–540.

<https://doi.org/10.1016/j.ensm.2019.07.005>.

- [42] A. Khataee, E. Dražević, J. Catalano, A. Bontien, Performance optimization of differential pH quinone-bromide redox flow battery, *J. Electrochem. Soc.* 165 (2018) A3918–A3924. <https://doi.org/10.1149/2.0681816jes>.